THE ASTRONOMICAL JOURNAL VOLUME 109, NUMBER 3 MARCH 1995

THE GLOBULAR CLUSTER SYSTEM OF M81

JEAN-MARC PERELMUTER[1]
Department of Physics and Astronomy, The Johns Hopkins University, Baltimore, Maryland 21218
Electronic mail: jperel@astro.umontreal.ca

RENÉ RACINE
Département de Physique, Université de Montréal and Observatoire du Mont Mégantic, Montréal PQ H3C 3J7, Canada
Electronic mail: racine@astro.umontreal.ca

Received 1994 October 7; revised 1994 November 1

ABSTRACT

We have obtained photometric BVR, morphological, and astrometric information on 3774 objects located within a 25′ radius of M81. This catalogue is complete for $15 \leqslant V \leqslant 21$; it is used here to identify globular cluster candidates in M81 and as a database for a statistical analysis of the system as a whole. The M81 globular cluster system is revealed as a strong surface density excess of ~70 objects within an 11 kpc galactocentric radius. The total population is estimated at $N_T = 210 \pm 30$ globulars. The spatial, $(B-V)$, and $(V-R)$ distributions are very similar to those of the Milky Way and of M31. Small but significant systematic errors in Madore *et al.*'s [AJ, 106, 2243 (1993)] photometry could be responsible for an overestimate of the Cepheid distance to M81 $[(m-M)_0 = 27.8]$ and we propose a revised modulus of $(m-M)_0 = 27.5 \pm 0.3$. The globular cluster luminosity function then reaches its maximum at $M_V^* = -7.5 \pm 0.4$, as it does in the galaxy and in M31. There is suggestive evidence that 13±5 objects are globulars seen through the disk of M81; spectroscopy or high-resolution imaging will resolve this issue. Using the $(B-R)_0$ index to trace [Fe/H], we notice a weak dependence of mean metallicity on galactocentric distance, as observed in the galaxy and in M31. This result argues in favor of *in situ* globular formation during the continuous collapse and self-enrichment of an early-type spiral host.

1. INTRODUCTION

This paper reports on an ongoing project to detect and characterize a globular cluster system in M81, a large, relatively nearby spiral galaxy, and to supplement the globular cluster system (GCS) data provided by our own galaxy and M31. At distances further than 2 Mpc, recognizing clusters on the basis of image structure on wide field survey images becomes impractical because their diameters are comparable to the seeing disk. Even at the distance of M31 ($D \simeq 720$ kpc; van den Bergh 1991), a large fraction of the Battistini *et al.* (1987) sample of nonstellar cluster candidates turned out to be background galaxies (Racine 1991; Racine & Harris 1992). Most globular clusters in the Local Group may be identified based on their image structure. Globulars at larger distances are generally detected as a statistical excess around a host galaxy, and some are identified from their radial velocity or spectral signature (Perelmuter *et al.* 1995). This task is very time consuming and limited by the efficiency of the spectrograph. For example, only recently has the halo GCS of M31 been cleaned of extraneous objects and sufficiently sampled to allow a secure comparison with the Milky Way GCS (Racine & Harris 1992; Huchra 1993). But the bounty far outweighs the striving. In broad terms, globular clusters serve to date galaxies, their distribution and kinematic bear witness to galactic formation, and their abundances test merger and accretion theories (e.g., Brown *et al.* 1991; Ashman & Zepf 1992; Brodie 1993). Whether the galactic halo formed from a gaseous monolith or is the product of accretions of smaller dwarf galaxies is still an unresolved dilemma (cf. Eggen *et al.* 1962; Searle & Zinn 1978; Sandage 1990; Zinn 1990). The similarities between the M31 and the Milky Way GCS are suggestive of a basic formation mechanism, while the birth of the gigantic M87 GCS ($N \sim 16\,000$) has been a controversial issue (Brodie & Huchra 1991; Djorgovski & Santiago 1992; Belov 1993; McLaughlin *et al.* 1994).

One of the best candidates for an additional GCS in a spiral galaxy is M81(NGC 3031), a large Sab spiral, of similar type and dimension as M31 (Sb) and the galaxy (Sbc). At ~3.2 Mpc (Freedman & Madore 1988; Jacoby *et al.* 1989; Madore *et al.* 1993; Freedman *et al.* 1994) M81 is too distant for its globular clusters to be resolved with ease, yet too close for its GCS to clearly stand out against the vast number of objects in the wide field it covers. Furthermore, its inclination ($i = 59°$) makes it difficult to detect objects over the bright disk background. However, it is the nearest large spiral outside the Local Group, and as will be shown later, its inclination allows the study of disk opacity. In M81, one must combine an ensemble of criteria to obtain the promised treasure from a population of thousands of extraneous objects.

We use an extensive database that includes photometric, astrometric, and morphological information on 3774 objects spread over a 50′ diameter field centered on M81 (RA_{J2000}=09:55:33.8, DEC_{J2000}=+69:03:54). Our goal is to maximize the success rate of the candidate list for ongoing

[1]Guest Observer, Kitt Peak National Observatory. KPNO is operated by AURA, Inc., under contract to the National Science Foundation.

TABLE 1. CFHT Plates of M81.

Plate ID	Epoch	Emulsion	Filter	Seeing	Exposure	Observer
A241	1980.28	098	RG630	~1.0"	60 min	van den Bergh
A236	1980.29	IIaD	GG495	~1.5"	60 min	van den Bergh
A008	1981.08	IIaO	GG385	~1.0"	45 min	Cayrel
A3664	1984.00	IIIaF	GG495	~0.7"	60 min	Racine

spectroscopic observations and to optimize the globulars' signal in the still contaminated sample for a preliminary study of the system. We show that we were successful in both undertakings.

The observations are described in Sec. 2. In Sec. 3 we discuss the reddening in M81 and determine *BVR* parameters of galactic-type globulars located in M81. Finally, in Sec. 4, candidates are selected in *BVR* space. The total population of the M81 GCS is estimated from its radial distribution. We also construct the globular cluster luminosity function and examine the distribution of [Fe/H], calculated from $(B-R)_0$.

2. OBSERVATIONS

2.1 Data

Our survey covers a 25′ radius field around M81 in B,V, and R broadband filters at two epochs, 1980.55 and 1990.17. The early epoch data are based on three plates obtained at the prime focus of the Canada–France–Hawaii Telescope (see Table 1). The 1980 plates were digitized at the David Dunlap Observatory using a Perkin-Elmer PDS microdensitometer. A 1984 plate taken in superior seeing was used to examine image structures but not included in the proper motion survey because its epoch is too different from 1980 and 1990. The late epoch is made up of 2048×2048 0.54″/pixel CCD frames obtained at prime focus of the Mayall 4 m telescope at Kitt Peak National Observatory on 1990 February 28, March 1 and 2.

Figure 1 shows the area covered by the survey. Objects detected in all three CCD frames and in all three plates are marked by filled circles; those with images on all three CCD frames but one or two plates only are shown as dots. The shadow of guiding probes can be seen due south and southwest of the galaxy. Although photometry was obtained for all objects in the field, we excluded those within a 1′ radius of the center to insure the quality of the photometry. The region covered by Holmberg IX, a small dwarf galaxy ~12′ east of M81, was removed from the survey to avoid background field contamination; it is shown as a doted circle in Fig. 1. Thus, although not all objects appear on all three plates, full coverage is regained by tolerating two plates overlap instead of three.

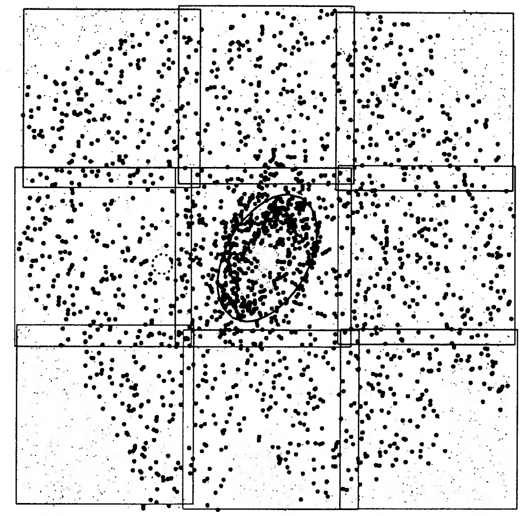

FIG. 1. The nine CCD fields mosaic is shown traced by solid lines. Each frame is 18 arcmin ×18 arcmin. Filled circles are objects detected on all three CCDs and all three plates; small dots were detected on all three CCDs and at most two plates. The disk of M81 is delineated by a thick solid ellipse.

2.2 CCD Photometry

2.2.1 Calibration

Standard stars in the galactic globular clusters NGC 4147, NGC 4374, NGC 2419, and M92 were observed each night before and after the M81 observations for photometric calibration in 1990; exposures were 300 s in B, 40 s in V, and 30 s in R. The airmass ranged from 1.1 to 1.4 for the standard fields and 1.3 to 1.5 for M81 fields. Calibrated magnitudes for the standard fields were kindly made available by Lyndsey Davis, whose CCD photometry is tied to the Landolt system. Aperture corrections were determined for each frame based on bright isolated stars. All the photometry was performed using DAOPHOT in IRAF. Figure 2 shows the comparison between Davis' standard and our instrumental values corrected for extinction using KPNO mean extinction coefficients ($k_b=0.23$, $k_v=0.16$, and $k_r=0.10$, NOAO 1990). Each night is represented in Fig. 2 by a different symbol: dots for night 1, crosses for night 2, and triangles for night 3. The agreement is excellent and demonstrates that the nights were photometric. Transformation equations from our instrumental b,v,r to standard B,V,R magnitudes were obtained from least squares of stars with $V\leqslant 18$:

$$V-v_0=0.040[(b-v)_0-1.50]-3.156, \quad \sigma=0.026, \quad n=128, \qquad \begin{matrix}\pm 0.006 & \pm 0.002\end{matrix} \tag{1}$$

$$(B-V)-(b-v)_0=0.003[(b-v)_0-1.50]-0.734, \quad \sigma=0.030, \quad n=125, \qquad \begin{matrix}\pm 0.007 & \pm 0.003\end{matrix} \tag{2}$$

$$(V-R)-(v-r)_0=0.003[(v-r)_0-0.80]-0.405, \quad \sigma=0.031, \quad n=126, \qquad \begin{matrix}\pm 0.013 & \pm 0.003\end{matrix} \tag{3}$$

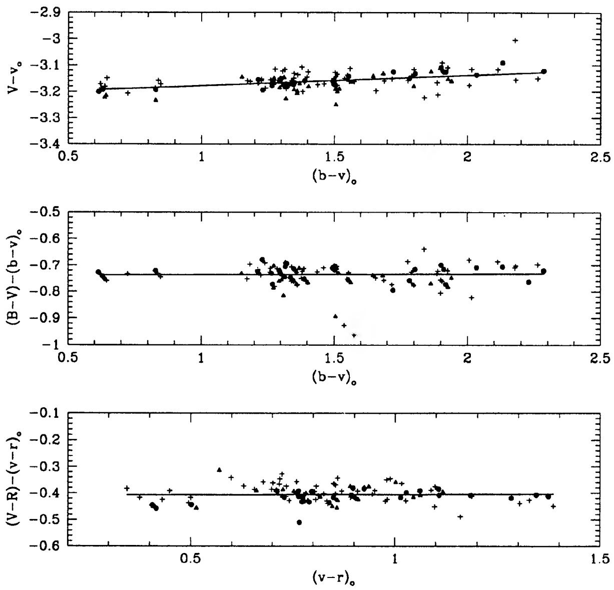

FIG. 2. Photometric calibration to standards in galactic globulars observed by L. Davis. Data from the three nights are consistent to 0.05 mag. Dots =1990 Feb. 28, crosses=March 1, triangles=March 2. The zero points and color terms of the present photometry are seen to be firmly established.

Figure 2 and the derived uncertainties of these transformation equations demonstrate that our photometry is accurately mapped onto the standard system: ± 0.003 in zero points and ± 0.01 in color coefficients.

In the peripheral M81 fields, magnitudes were derived using the APPHOT package, which directly accumulates pixel counts. We paid special attention to the central field which contains the M81 disk and where crowding and background fluctuations are severe. A two phase method of reduction was applied, following Fisher *et al.* (1990). Objects are detected, their brightness measured, and they are subtracted from the image by a scaled template point spread function. This was done to generate a *mask* frame to subtract background fluctuations. Bad pixels were edited by hand using nearby pixels. A median filter was then applied to the frame, first with a $2.7'' \times 2.7''$ box, followed by a $4.3'' \times 4.3''$ box. The choice of the box size was made after experimenting with different size boxes; this particular set maximizes both the smoothing while still retaining the structure of the disk. The ALLSTAR procedure was then repeated on the background subtracted frames. Artificial stars (30) were added in the original frames; no significant difference was found in their magnitude measured *before* and *after* sky subtraction, $\sigma = 0.02$ mag.

TABLE 2. Magnitude limit of BVR images.

Filter	Exposure	$MAG_{99\%}$
B	3600 sec	23.0
V	360 sec	21.5
R	120 sec	20.5

TABLE 3. Photometric internal errors.

	σ_V	σ_{B-V}	σ_{V-R}
$V<20$	0.07	0.03	0.03
$20 \leq V \leq 21$	0.08	0.07	0.06

The limiting magnitudes in B,V, and R to 99% completeness were determined by adding and retrieving artificial stars using ADDSTAR and FIND in DAOPHOT. The results are given in Table 2 for the average of 10 runs of 20 artificial stars added at a time. The B frames reach the deepest magnitudes; the magnitude limit is mostly imposed by the shallower R images. The fraction of stars retrieved was radially uniform to within $2'$ from the center, whereupon the bright galactic background significantly hampers detection.

2.2.2 *Photometric errors*

All the photometry in this survey is based on the 1990 KPNO CCD frames. The main source of photometric uncertainty is due to the lower signal to noise of fainter images. Though the brighter disk background lowers the signal-to-noise ratio, DAOPHOT errors are not significantly affected beyond $1'$ from the center of M81. Objects with $V=20-21$ and beyond $1'$ have $\langle \sigma_{\rm DAOPHOT} \rangle (B,V,R) \simeq 0.05$ mag, while inside $1' \langle \sigma_{\rm DAPHOT} \rangle \simeq 0.15$, 0.12, 0.10 mag in B,V, and R, respectively, and for the same range in V.

We use objects in the overlapping regions of the CCD mosaic to measure the internal consistency in the photometry. They are shown in Table 3 and in Fig. 3 as a function of magnitude V. The V, $(B-V)$, and $(V-R)$ zero points are consistent from field to field within 0.02 mag. The dispersions are uniform to $V \simeq 20$; at fainter magnitudes there is a steep increase in photometric uncertainties.

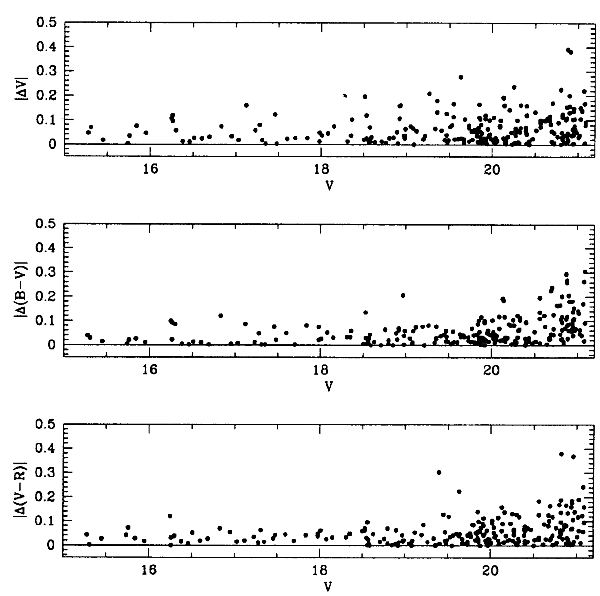

FIG. 3. Magnitude and color differences, as a function of V, for objects in the overlap region of the CCD mosaic.

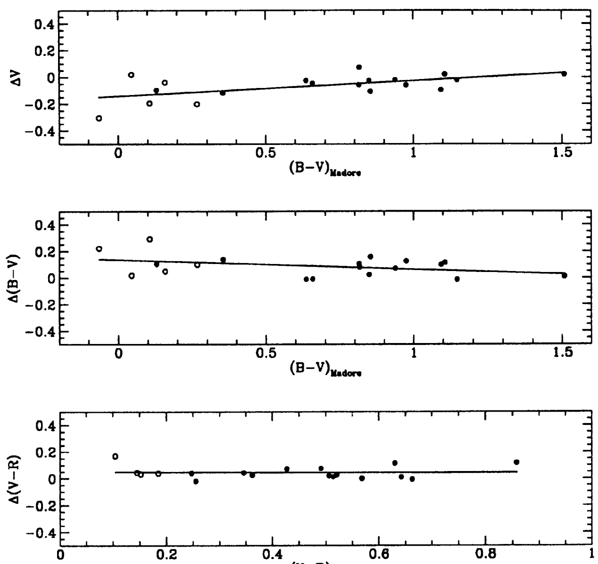

FIG. 4. Photometric comparison to Madore *et al.* (1993). The difference is this paper Madore as a function of $(B-V)$ or $(V-R)$ Madore. Filled circles have $V \leqslant 20$ and open circles have $20 < V < 21$. Significant color terms are visible.

2.2.3 *Comparison with previous photometry*

We limit this discussion to the comparison of our data to those recently published by Madore *et al.* (1993) and based on deep CFHT CCD frames ($V_{\rm lim} \sim 23.0$, cf. their Figs. 5 and 6). We show in Fig. 4 the differences in V, $B-V$, and $V-R$ as a function of magnitude; objects brighter than $V<20$ are shown as filled circles and those fainter are shown as open circles. The agreement is reasonably good (within 0.1 mag), but significant color trends are present in V and $(B-V)$. The least squares fit gives

$$\begin{aligned} \Delta V &= +0.116[(B-V)_M - 0.80] - 0.050, \\ &\quad \sigma = 0.07, \quad n = 21, \\ &\pm 0.040 \quad \pm 0.019 \end{aligned} \tag{4}$$

$$\begin{aligned} \Delta(B-V) &= -0.072[(B-V)_M - 0.80] + 0.078, \\ &\quad \sigma = 0.07, \quad n = 20, \\ &\pm 0.040 \quad \pm 0.018 \end{aligned} \tag{5}$$

$$\begin{aligned} \Delta(V-R) &= -0.008[(V-R)_M - 0.4] + 0.046, \\ &\quad \sigma = 0.05, \quad n = 18, \\ &\pm 0.056 \quad \pm 0.012 \end{aligned} \tag{6}$$

where the difference is this photometry-Madore's as a function of Madore's $(B-V)_M$ or $(V-R)_M$ index. The dispersions in Eqs. (4)–(6) result from the convolution of random errors in both photometric series and is dominated by objects with $18 \leqslant V \leqslant 20$. The uncertainty quoted for each of the coefficients in Eqs. (4), (5), and (6) is the quadratic sum of the errors of the fits in Fig. 4 and of the uncertainties in our calibration to the standard system [Eqs. (1), (2), and (3)].

TABLE 4. Astrometric errors in mas yr^{-1}.

	V≤18.50	18.75	19.25	19.75	20.25	20.75
$\sigma_{1990}(n_{CCD}=3)$	1.1	1.2	1.3	1.5	2.0	2.6
$\sigma_{1980}(n_{plates}=3)$	2.0	2.3	2.7	3.5	4.3	5.7
$\sigma_{1980}(n_{plates}=2)$	-	2.2	3.7	7.8:	6.2	6.4:
$\sigma_{1980}(n_{plates}=1)$	3.5	4.0	4.7	6.1	7.4	9.9

Equations (4), (5), and (6) therefore indicate that Madore *et al.*'s (1993) photometry contains small but significant systematic errors both in color coefficients, for V and $(B-V)$, and in zero points at $(B-V) \sim 0.8$ and $(V-R) \sim 0.4$. We note, in particular, that at these intermediate colors, Madore *et al.*'s $(B-V)$ and $(V-R)$ indices are too blue and by amounts whose ratio is, coincidentally, close to the ratio $E(B-V)/E(V-R)$ expected from interstellar reddening. Thus, the use of Madore *et al.*'s photometry to determine the reddening of intermediate color objects, such as Cepheid variables in M81, would underestimate $E(B-V)$ by 0.08 ± 0.02 mag and A_V by 0.25 ± 0.06 mag. Since that same photometry also leads to V magnitudes which are too faint by 0.05 mag [Eq. (4)], the distance modulus derived from the M81 Cepheids would be 0.30 ± 0.07 too large. Therefore, we propose to revise their M81 distance modulus from $(m-M)_0 = 27.8$ to $(m-M)_0 = 27.5 \pm 0.3$.

2.3 *Astrometric Solutions*

2.3.1 *Intraepoch solutions*

A ten-geometric term astrometric solution was calculated for each of the nine CCD fields separately. This allowed for field distortions to be modeled by the plate solution. Magnitude and color terms were found to be negligible. Mean 1980 and mean 1990 positions were defined as the average centroids within each epoch. The standard errors σ_{1980} and σ_{1990} of the mean 1980 and 1990 position were determined for each object on the basis of the internal consistency of the measured positions by

$$\sigma_{1980,90} = \sqrt{\frac{\Sigma(\bar{x}-x)^2 + \Sigma(\bar{y}-y)^2}{2n(n-1)}}, \tag{1}$$

where x and y are the positions at given epoch in B, V, or R; $\bar{x}$ and $\bar{y}$ are their means and n is the number of plates or CCD frames the object has been detected upon. Were retained those objects that appear on all three CCD frames, so that $n_{1990} = 3$, whereas $n_{1980} = 1$, 2, or 3 because some of the 1980 plates are not as deep as the CCD frames. We compare in Table 4 the overall 1980 mean error (mas yr^{-1}) for $n_{\rm plate} = 1$, 2, or 3 to that of 1990, which has $n_{\rm CCD} = 3$, as a function of magnitude. Entries for objects detected on two plates have a higher degree of uncertainty because of small numbers in each bin. To estimate the 1980 centroid error when only one plate measure was available, $n_{1980} = 1$, the mean error $\sigma_{1980}(n_{1980} = 3)$ was rescaled by $\sqrt{3}$.

2.3.2 *Interepoch solutions*

Overlap between 1980 and 1990 positions was performed using a ten-term plate solution also on a per field basis, for the same optical considerations as in the intraepoch case. The

TABLE 5. Matching rates for stellar objects.

	V=16-18	18-19	19-20	20-21	16-21
CCD Objects	202	157	325	618	1302
$N_{Plates} \geq 1$	1.00	1.00	1.00	1.00	1.00
$N_{Plates} \geq 2$	1.00	0.99	0.99	0.94	0.97
$N_{Plates} \geq 3$	1.00	0.97	0.95	0.78	0.88

matching radius was set to 0.5″ during the computation of the plate solution, and it was increased to 10.0″ to produce the final output catalogue. Proper motions are therefore limited to $\mu \lesssim 10$ arcsec/10 yr=1 arcsec yr^{-1}. A rotation between the orientation of the plates and the orientation of the CCD mosaic limits their overlap to within 23′ of M81 in the case of $n_{1980}=3$ and to 25′ for $n_{1980}<3$ (see Fig. 1). The 1980–1990 overlap success rate is given in Table 5 divided in three magnitude ranges and for objects detected on at least 1, 2, or 3 plates. The sample used for this table was constrained to a 20′ radius to exclude those regions shadowed by the guiding probe, as seen in Fig. 1. No correlation was found between overlap rate and distance to M81 (at $\gtrsim 2'$ from its center). In effect, all objects detected on all three CCD frames are found on at least one plate.

The total error in the proper motion is the convolution of Eq. (7) for both epochs,

$$\sigma_\mu = \frac{\sqrt{\sigma_{1980}^2 + \sigma_{1990}^2}}{\Delta T}, \tag{2}$$

where $\Delta T = 9.62$ yr.

The variation of the total astrometric accuracy, σ_μ, is shown in Fig. 5 as a function of magnitude and for two annuli centered on M81, using *stellar* images with $n_{\text{plates}} \geq 1$. Error bars represent the standard error on the average σ_μ. At

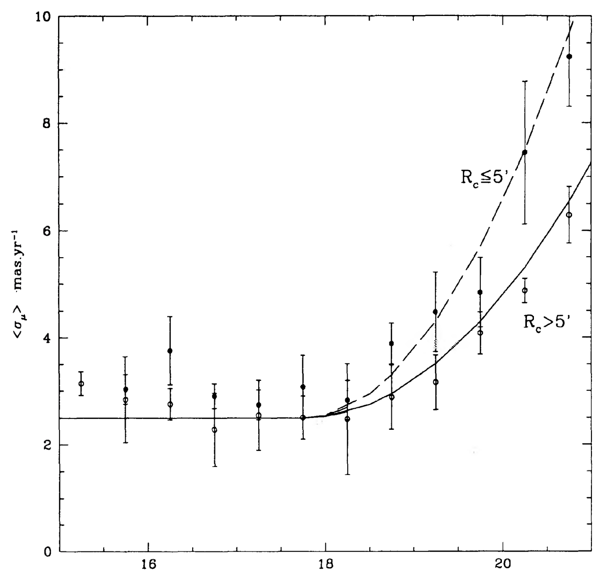

FIG. 5. The variation of the mean astrometric uncertainty as a function of magnitude. The uncertainty for objects over the bright disk background at $R \leq 5'$ (filled circles, dash line) rises faster than for those outside of $R = 5'$ (open circles, solid line).

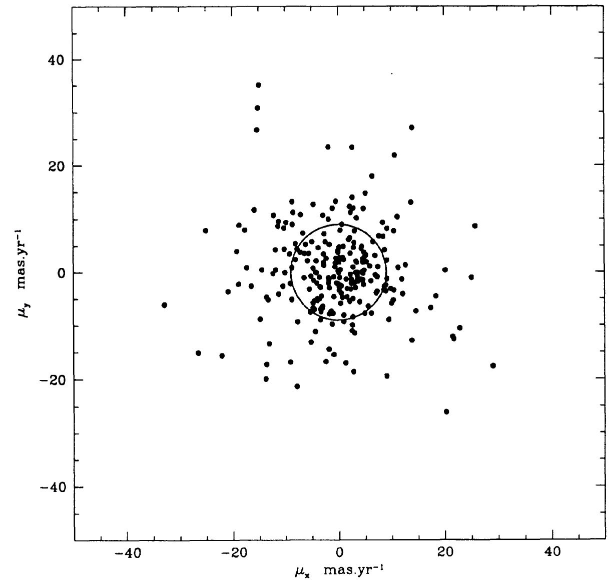

FIG. 6. The (μ_x, μ_y) diagram for objects used to establish the absolute zero of proper motion. The circle has radius $2\sigma = 9$ mas yr^{-1}.

$V<17.75$, no significant difference in the mean astrometric precision is visible with galactocentric or magnitude. However, at fainter magnitudes the inner ($R_c \leq 5'$) and the outer ($R_c > 5'$) samples exhibit a magnitude dependent increase in σ_μ. At $R_c \leq 5'$ the relation steepens with increasing V probably caused by the brighter background of the disk,

$$\sigma_\mu(\text{mas yr}^{-1}) = 2.5, \quad V \leq 17.75 \quad \text{all } R_c, \tag{3}$$

$$\sigma_\mu(\text{mas yr}^{-1}) = 2.5 + 0.80(V - 17.75)^2, \quad V > 17.75 \quad R_c < 5', \tag{4}$$

$$\sigma_\mu(\text{mas yr}^{-1}) = 2.5 + 0.45(V - 17.75)^2, \quad V > 17.75 \quad R_c \geq 5'. \tag{5}$$

2.3.3 *The absolute zero of proper motion*

The zero of proper motion was established from the location in μ space of visually identified galaxies that are circular with a well defined core and $V \leq 20$ to insure good centering, and of "globular-like" objects (cf. Sec. *4.1.1*). Zero points were determined for each field using ~25 objects per field. In Fig. 6 we plot (μ_x, μ_y) of the 265 objects used in establishing $\mu=0$ with a circle of radius $2\sigma_{\mu=0} = 9$ mas yr^{-1}; where $\sigma_{\mu=0}$ represents the scatter of μ about the origin, that is, the precision of the absolute referencial for the survey as a whole. For each field, the absolute zero proper motion is defined with a precision of $\sigma_{\mu=0}/\sqrt{N-1} = 0.9$ mas yr^{-1} ($N = 25$), comparable to the NPM Lick survey (Klemola *et al.* 1987; Hanson 1987).

2.4 *The μ/σ_μ Distributions*

Group membership in proper motion studies is generally established in relation to a threshold which is a function of the overall precision, for example, $\mu_{\text{thresh}} = 2\langle\sigma_\mu\rangle$. This is eas-

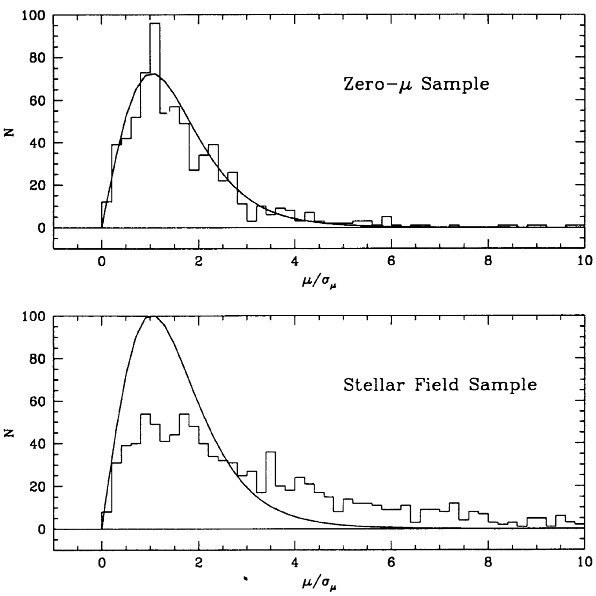

FIG. 7. The distribution of μ/σ_μ for the zero-μ sample (top) and for field stars away from M81 (bottom). The zero-μ distribution is well fit by a Moffat (1969) function with β=4.5, normalized to the total population of the histogram. This is expected for a sample with proper motions dominated by random measuring errors. Whereas the μ/σ_μ histogram for objects away from M81 is not well fitted by a normalized Moffat function. These objects have significant astronomical proper motions.

ily applied when $\langle\sigma_\mu\rangle$ is not affected by other parameters in the survey. In our case, it is preferable to decide membership from the value of μ/σ_μ because it measures the statistical significance individually. A sample drawn on that basis maintains uniformly significant proper motions.

To find the intrinsic μ/σ_μ distribution of zero-μ objects, we use those objects which define the absolute zero in μ space and faint blue objects over the M81 disk (e.g., $B-R$ <0.8 and $R_c<10'$). The sample of blue stars is largely dominated by objects in M81 and thus representative of a zero-μ population. We show in Fig. 7 (top) the μ/σ_μ histogram for this zero-μ sample. A field sample is shown in Fig. 7 (bottom) using *stellar* images at $R_c>15'$, thereby exclusively sampling the field. The zero-μ distribution peaks at $\mu/\sigma_\mu=1$ because the proper motions are purely due to random measuring errors. A chi-square statistic suggests the Moffat (1969) distribution with β=4.5 provides the most accurate fit; it is plotted normalized to the total population in Fig. 7 (top). A Kolmogorov–Smirnov statistic cannot reject the null hypothesis of the same parent population at the 99.5% confidence level. That a Moffat is a more precise description of the astrometric error function than a Gaussian is consistent with its higher accuracy in fitting stellar light profiles (Moffat 1969). The addition of galactic stars with significant proper motions to the zero-μ sample has the effect of filling the tail end of the μ/σ_μ distribution, as seen in Fig. 7 (bottom). The KS test rejects the hypothesis of a same parent population with the normalized Moffat at >99.9% confidence. This is due to the real proper motions of galactic stars. Figure 7 shows that the accuracy of our proper motion

TABLE 6. Catalogue of objects in the M81 field.

ID	RA(2000)	DEC(2000)	Epoch	V	B-V	V-R	N_{plate}	μ_l	μ_b	μ/σ_μ
80251	09:50:52.829	69:06:42.42	1988.3	20.80	1.68	0.81	2	0	20	4.2
80240	09:50:53.019	69:07:59.87	1986.1	20.32	1.13	0.64	3	7	2	1.4
80249	09:50:53.265	69:06:46.63	1988.5	20.43	1.74	0.87	2	-5	13	1.8
80224	09:50:54.148	69:09:17.65	1990.1	19.09	0.84	0.51	0	0	0	0.0
80225	09:50:55.337	69:09:17.31	1990.1	21.08	1.57	0.69	0	0	0	0.0
80259	09:50:55.514	69:06:14.00	1988.5	20.78	1.78	0.85	2	22	13	2.8
70128	09:50:55.660	69:19:04.25	1990.1	15.45	1.04	0.58	0	0	0	0.0
70124	09:50:55.750	69:19:13.56	1990.1	16.65	0.79	0.45	0	0	0	0.0
70347	09:50:55.845	69:16:26.39	1990.1	20.81	0.78	0.25	0	0	0	0.0
70140	09:50:55.924	69:17:52.87	1990.1	19.38	1.69	1.60	0	0	0	0.0
80257	09:50:56.077	69:06:18.72	1985.1	20.13	1.58	0.84	2	4	24	7.3
80262	09:50:56.115	69:05:53.15	1988.6	19.87	1.68	1.05	2	3	10	1.6
70237	09:50:56.585	69:26:42.62	1990.1	20.06	1.58	0.79	0	0	0	0.0
80236	09:50:56.849	69:08:42.16	1982.8	16.72	0.78	0.39	3	10	2	2.2
80273	09:50:57.234	69:04:14.85	1987.1	21.16	0.95	0.59	2	0	0	0.0
80329	09:50:57.689	68:57:35.22	1989.8	20.80	1.40	1.15	3	-5	10	2.0
80275	09:50:58.260	69:04:13.39	1989.6	19.34	1.29	0.68	2	17	-3	1.2
80363	09:50:59.053	69:04:04.62	1987.3	20.38	0.71	0.18	3	-7	-3	2.1
70340	09:50:59.093	69:24:17.45	1990.1	19.66	1.47	0.88	0	0	0	0.0
80372	09:50:59.268	68:59:18.92	1981.5	19.11	1.09	0.64	3	6	0	1.4
80199	09:51:00.421	69:12:11.58	1990.1	21.02	1.48	0.90	0	0	0	0.0
80223	09:51:00.606	69:09:18.16	1990.1	20.98	1.48	0.76	1	27	43	10.3

survey is sufficient to recognize as such a large fraction of individual galactic stars. The study of their kinematics is presented in a following paper (Racine & Perelmuter 1995). The catalogue of all 3774 objects is available on ApJ/AJ CD-ROM; a sample of its presentation is given in Table 6 for guidance regarding its form and content. The first column gives an identification number; the RA and the DEC are given in columns 2 and 3 at epoch J2000.0 based on the *HST*-GSC; column 4 is the mean epoch of observation for the combined plate(s) and CCD images; columns 5–7 are the *BVR* photometric indices; in column 8 we give the number of plates the object has been detected upon; columns 9–10 are the proper motion (mas yr^{-1}) in the galactic coordinate system; column 11 gives the level of significance of the total proper motion, $\mu = \sqrt{\mu_l^2+\mu_b^2}$.

3. THE GLOBULAR CLUSTER *B,V,R* AND MORPHOLOGY MANIFOLD

3.1 Global Strategy

The small size of globular clusters, $r_t \leqslant 40$ pc, limits the distance range of their visual identification with ground-based telescopes. Racine (1991), Racine & Harris (1992), and Reed *et al.* (1992, 1994) demonstrated the necessity to combine *BVR* colors and morphology to establish membership to the M31 halo GCS. That system was found to have *BVR* parameters very similar to those of the galactic GCS.

Based on the assumption that M81 globular clusters resemble the galactic and M31 populations in their range of parameters, we draw a list of candidates from the database described in Sec. 2. Since Milky Way and M31 globulars fall in a unique and well defined region of the $(BVR)_0$ plane, we extrapolate their V, $(B-V)$, and $(V-R)$ ranges to the distance and reddening of M81. Both a *nonstellar* and a *stellar* catalogue of candidates, satisfying *BVR* criteria of membership, are studied. The contamination of galactic stars in the *stellar* sample is reduced with the addition of the μ/σ_μ proper motion criterion.

The following analysis assumes the Cepheids distance modulus *corrected* for the color trends found in Madore *et al.*'s (1993) photometry and which we revised in Sec.

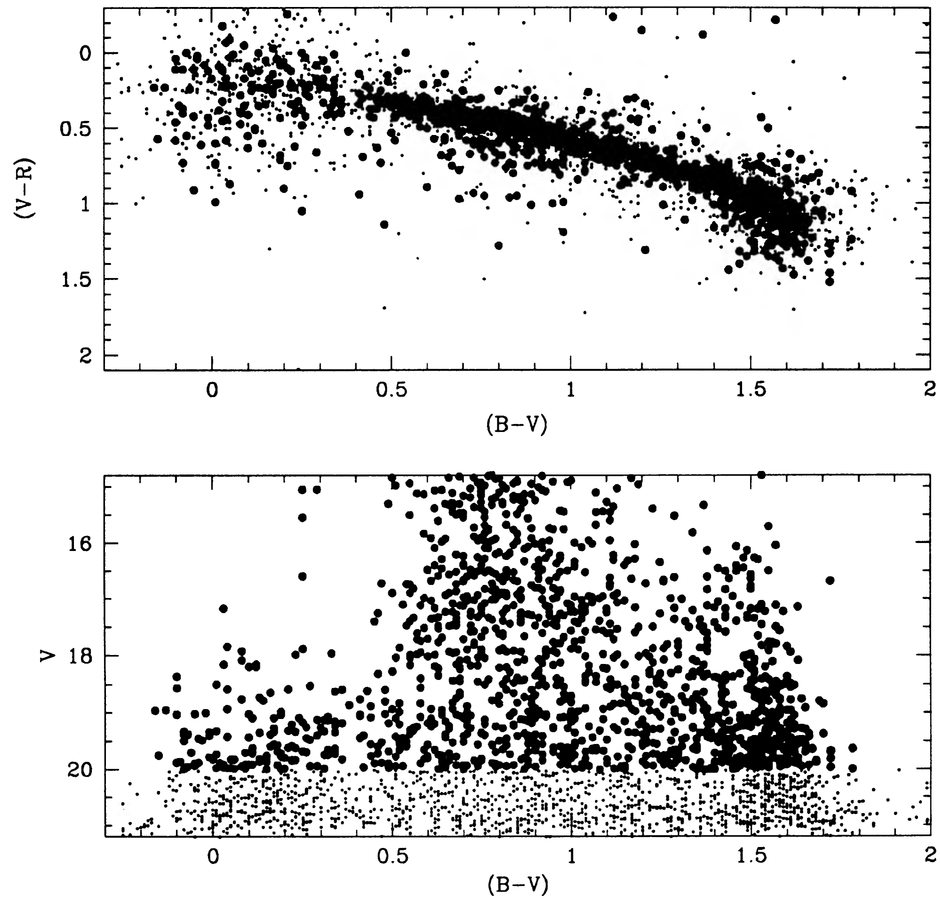

FIG. 8. The color–color and color–magnitude diagrams for all star-like objects in the survey. Filled circles have $V<20$ and dots have $V \geqslant 20$.

2.2.3 to $(m-M)_0=27.5\pm0.3$. This corresponds to d(M81) $=3.2\pm0.4$ Mpc; the linear and angular sizes are thus related by 1 arcmin$=0.9\pm0.1$ kpc.

3.2 Foreground Reddening

We show in Fig. 8 the color–color (a) and the color–magnitude (b) diagrams for all objects in the survey excluding asymmetric and amorphous images. Filled circles are objects with $V \leqslant 20$, while the dots have $V>20$. The break at $(B-V)=0.53\pm0.03$ is identified with the main-sequence turnoff, $(B-V)_{\mathrm{TO},0}$, reddened by the Milky Way. The intrinsic location is a function of metallicity ranging from $(B-V)_{\mathrm{TO},0}=0.37$ for M92 to 0.48 for 47 Tucanae (Hesser *et al.* 1987; Stetson & Harris 1988). Faint M81 field stars likely belong to a (moderately) metal poor, old stellar population. An estimate of the reddening can be made by comparing the observed turnoff to the mean intrinsic value determined from M92, M15, M68, M13, and 47 Tucanae, $\langle(B-V)_{\mathrm{TO},0}\rangle=0.40\pm0.03$, implying $\mathrm{E}_{(B-V)}$(Foreground) $=0.13\pm0.05$. Estimates of the galactic reddening in the direction of M81 have also been obtained by Burstein & Heiles (1984) and Kaufman *et al.* (1987), yielding $\mathrm{E}(B-V)=0.04$ and 0.10 ± 0.03 based on H I column density and 100 μm intensity measurements, respectively. We adopt the average of these three estimates for the foreground reddening in the direction of M81, $\mathrm{E}_{(B-V)}$(Foreground)$=0.09\pm0.04$.

3.3 Total Reddening

A summary of *total* reddening determinations in M81 (foreground plus M81 contributions) is given in Table 7. The value derived by Freedman *et al.* (1994) and based on Madore's photometry is ~0.25 mag lower in $\mathrm{E}(B-V)$ than other estimates (except for the uncertain UV data). The discrepancy between the Cepheid (Madore *et al.* 1993; Freedman *et al.* 1994) and the red supergiant data (Humphrey *et al.* 1986) is surprising because one would expect similar sites for both populations. However, correcting for the systematic trends found in Madore *et al.*'s (1993) photometry

TABLE 7. Total reddening for M81.

E(B-V)	Method	Source
0.19±0.2	UV continum imaging of M81	Bruzual *et al* (1982)
0.35†	JHK photometry of M supergiants	Humphreys *et al* (1986)
0.36±0.1	Hα and Radio continuum	Kaufman *et al* (1987)
0.40†	Color of blue stars in M81/NGC2403	Zickgraf and Humphreys (1991)
0.11*	Cepheids differential modulus M81-LMC	Freedman *et al* (1994)
0.38±0.1	Position of blue plume	This paper
0.32±0.1	HI column density over the face of M81	This paper

Notes to TABLE 7:

†) mean of the quoted values.

*) assuming $(\mathrm{m-M})_o^{LMC}=18.5$ and $\mathrm{E}_{B-V}^{LMC}=0.17$.

[Eqs. (4)–(6)] would decrease this dichotomy to ~0.1 mag, within the photometric uncertainties. We also estimate the reddening from the median color of early type (OB) supergiants in the CMD of M81, [Fig. 8(b)]. OB supergiants make up a *blue plume* which should be centered at $(B-V)_0=-0.3$ (Flower 1977). The *blue plume* is defined as including all objects in M81 with $B-V<0.3$ to avoid inclusion of main sequence and evolved stars in M81. The fainter objects in Fig. 8(b) have $V\leqslant 21$, if these objects were part of M81, they would have $M_V<-7$. At such magnitudes, only supergiants and globular clusters could be visible in M81. We find the median color of the *blue plume* $(B-V)_{\rm Plume}=0.08\pm0.01$ ($\sigma=0.10$, $N_{\rm Stars}=269$). For an unreddened blue plume color $(B-V)_0=-0.30$ (Flower 1977) we derive from our data a median $E(B-V)=0.38\pm0.07$ of which 0.29 ± 0.08 is due to M81. The method also indicates that variations in the optical path within M81 cause a 0.10 mag dispersion in $E(B-V)$. By comparison, Rots' (1975) H I maps of M81 show $N(\mbox{H I})=15\pm5\times10^{20}$ atoms/cm^2, implying $E(B-V)=0.32\pm0.10$ mag (using Bohlin *et al.* 1978). A blue plume reddening value may overestimate the actual excess because it assumes the intrinsic colors to be that of OB type stars only, while many objects must be multiple (Humphreys & Aaronson 1987), therefore spreading the intrinsic color range via later type stars' contribution to the integrated light; still, the flux must remain dominated by the brighter O-type stars.

Clearly, precise reddening estimates in M81 only take meaning *locally* because of inhomogeneities in the distribution of the dust column density. The purpose of Table 7 is to bracket total reddening estimates over the surface of the disk. The total mean reddening averaged through that table is $E(B-V) = 0.30 \pm 0.11$, and thus $E(V-R) = 0.20 \pm 0.07$ and $A_V = 0.93 \pm 0.34$ mag ($R_V=3.1$, Mathis 1990). The contribution of the M81 disk itself is $E(B-V)_{\rm M81disk} = 0.20 \pm 0.11$. This analysis is valid in a general context, such as in population studies, but is uncertain at the local level. For instance, adopting reddening values at the low end and then at the high end of the range $[\Delta E(B-V)\sim0.2]$ would propagate as a 25% difference in the distance. This effect may be responsible in part for the difference in the photometric distances of Sandage (1984), Zickgraf & Humphreys (1991), and Metcalfe & Shanks (1991), all using red supergiants.

3.4 The Expected Luminosity of the M81 Globulars

The intrinsic globular cluster luminosity function (GCLF) of the Milky Way and M31 halo have been shown by Racine & Harris (1992) to be very similar, with a peak at $M_V^* = -7.5 \pm 0.2$. The uncertainty takes into account a possible difference of 0.2 mag reported by Secker (1992), M31 being brighter. No notable difference can be found between the galaxy disk and halo GCLF (Armandroff 1989). The three first-rank globulars occur at $M_V\simeq-9.5$ in both the galaxy and M31. At $(m-M)_0^{\rm M81}=27.5\pm0.3$ (corrected Cepheids modulus), the brightest M81 globulars should appear at $V\gtrsim18$, with the peak of the luminosity function at $V^*=20.3\pm0.4$. At the survey's magnitude limit, $V=21$ mag, 86% of the total Milky Way GCS and 80% of the M31 halo GCS would be included at the location of M81; this implies a 83%±3% completeness in luminosity for this survey.

TABLE 8. Color indices of globular clusters.

	Galaxy	M31	Expected for M81†
M_V^*	-7.5±0.3	-7.5±0.3	20.30±0.40
$(B-V)_o$	0.69±0.10	0.70±0.14	0.80±0.10
$(V-R)_o$	0.42±0.05	0.41±0.07	0.50±0.06
N	80	69	-

Notes to TABLE 8:
†) assuming $(m-M)_0^{M81}=27.5$ and A_V(Foreground)=0.3

3.5 The Expected BVR Color of the M81 Globulars

Reed *et al.* (1992, 1994) note that M31 halo globulars scatter about the locus of the Milky Way globular population in the $(B-V)_0,(V-R)_0$ diagram and suggest using those indices as a classification scheme, in particular for the rejection of background galaxies. Perelmuter (1993a) also noted this effect and suggested a similar scheme in relation to foreground stars. However, contaminating objects exist within 0.1 mag of the globular cluster locus, which is on the order of photometric errors. Furthermore, due to the increase in photometric uncertainty with magnitude, fainter globulars are more likely to be scattered away from the main GC relation. Unless the dimension of the BVR box takes this effect into consideration, a magnitude bias may eventually plague the GCLF.

Using a database on galactic and M31 clusters, kindly provided by W. Harris, we calculated the mean $(B-V)_0$ and $(V-R)_0$ indices for the Milky Way and M31 halo GCS, given in Table 8. Also shown are the dispersions about the color indices and the error in the location of M_V^*. Interestingly, the scatter in $(V-R)$ reflects only the photometric uncertainties [cf. Reed *et al.* (1992, 1994) on M31 and Reed *et al.* (1988) on MW], while in $(B-V)$ there is an additional *cosmic* scatter, such that

$$\sigma_0(B-V)=0.10, \tag{6}$$

$$\sigma_0(V-R)\leqslant0.02. \tag{7}$$

We now convolve Eqs. (12) and (13) with the photometric uncertainties. Referring back to Table 3, we note an increase in the photometric error at $V>20$ mag. In order that the BVR box include all globulars independent of V, we convolve Eqs. (12) and (13) with the $\sigma(B-V)$ and $\sigma(V-R)$ which apply at the fainter magnitudes. The resulting $\pm3\sigma$ range in color indices is

$$V\geqslant18, \tag{8}$$

$$0.5\leqslant(B-V)\leqslant1.1, \quad \text{and } \sigma_{\rm M81}(B-V)=0.10, \tag{9}$$

$$0.3\leqslant(V-R)\leqslant0.7, \quad \text{and } \sigma_{\rm M81}(V-R)=0.06. \tag{10}$$

TABLE 9. Fraction of field stars retained to $(\mu/\sigma_\mu)_*$ and relative SNR of $\mu=0$ objects.

$(\mu/\sigma_\mu)_*$	$(1-f_*)$											$(1-f_{\mu=0})$	Q
	16.25	16.75	17.25	17.75	18.25	18.75	19.25	19.75	20.25	20.75	16-21		
0.5	0.05	0.00	0.11	0.03	0.08	0.00	0.12	0.30	0.30	0.80	0.06	0.10	0.41
1.0	0.05	0.06	0.21	0.12	0.16	0.12	0.29	0.21	0.25	0.23	0.18	0.32	0.75
1.5	0.05	0.12	0.26	0.24	0.24	0.35	0.50	0.41	0.38	0.50	0.29	0.56	1.03
2.0	0.14	0.18	0.32	0.39	0.32	0.47	0.68	0.52	0.59	0.69	0.40	0.56	1.17
2.5	0.27	0.21	0.34	0.52	0.52	0.53	0.76	0.59	0.66	0.73	0.47	0.74	1.24
2.75	0.24	0.26	0.34	0.51	0.46	0.39	0.72	0.63	0.73	0.78	0.51	0.90	1.26
3.0	0.32	0.32	0.37	0.55	0.56	0.53	0.76	0.76	0.78	0.77	0.54	0.92	1.25
3.5	0.50	0.38	0.47	0.64	0.64	0.76	0.76	0.79	0.84	0.81	0.63	0.96	1.21
4.0	0.64	0.50	0.50	0.73	0.72	0.88	0.79	0.83	0.84	0.81	0.69	0.98	1.18

3.5.1 The effect of the disk

In the range of colors adopted above, the opacity of the M81 disk will affect the observation of the M81 GCS: extinction by the disk would make objects appear fainter and redder.

For the average internal reddening derived in Sec. *2.1*, $E_{(B-V)}$(M81 disk) = 0.2, one derives for objects seen through the M81 disk $E_{(B-V)}$(through M81 disk)=0.5 and A_V(through M81 disk)=1.6 mag. The BVR box is affected as such,

$$V \geq 19.6, \tag{11}$$

$$0.9 \leq (B-V) \leq 1.5, \quad \text{for } \sigma_{\mathrm{M81}}(B-V)=0.10, \tag{12}$$

$$0.6 \leq (V-R) \leq 1.0, \quad \text{for } \sigma_{\mathrm{M81}}(V-R)=0.06. \tag{13}$$

3.6 Foreground Contamination

3.6.1 The proper motion criterion

Wyse's (1992) three-component galactic model predicts 497 Milky Way stars per sq deg in the $V,(B-V)$ range expected for M81 globulars [Eqs. (14) and (15)]. In that CM range we observe 518 objects per sq deg at $15' < R_c < 25'$. This radial range is meant to insure a fair representation of the field. Adding the $(V-R)$ criterion decreases the incidence of background galaxies, and the observed surface density decreases to 490 objects per sq deg. As we showed in Sec. *2.4*, a large number of galactic stars may be removed from a *stellar* GC candidate list on the basis of μ/σ_μ. The choice of the cutoff limit, $(\mu/\sigma_\mu)_*$, should maximize the fraction of stars rejected *and* minimize the exclusion of zero-μ objects at the tail end of their Moffat-like μ/σ_μ distribution. The best strategy is to maximize the *signal-to-noise* ratio of the resulting sample, which in this context we express as,

$$Q = \frac{(1-f_{\mu=0})}{\sqrt{1-f_*}}, \tag{14}$$

where $f_{\mu=0}$ and f_* are the fraction of zero-μ and galactic objects with $\mu/\sigma_\mu > (\mu/\sigma_\mu)_*$ (i.e., that are rejected). The numerator is calculated from a Moffat (β=4.5) distribution and the denominator is an observed quantity. Different values of Q are shown in Table 9 for a run of $(\mu/\sigma_\mu)_*$ in the V=16–21 interval; the observed fraction of objects in the *stellar* sample that are retained, $(1-f_*)$, is also given. We adopt the value $(\mu/\sigma_\mu)_*=2.75$ where the signal to noise Q reaches a maximum. At that limit, 90% of the zero-μ objects are retained.

TABLE 10. μ/σ_μ performance at $R_c<5'$.

	V≤18.5	18.75	19.25	19.75	20.25	20.75
$\overline{\sigma_\mu}(disk)/\overline{\sigma_\mu}(halo)$	1.0	1.02	1.15	1.33	1.48	1.59
$(\mu/\sigma_\mu)_{*,Eff.}$	2.5	2.6	2.9	3.3	3.7	4.0
$(1-f_{*,Eff})/(1-f_*)$	1.00	1.00	1.05	1.24	1.25	1.11

3.6.2 The efficiency of μ/σ_μ with V and R_c

We saw in Sec. *2.3.2* that astrometric uncertainties, σ_μ, increase for fainter objects and that this increase steepens over the bright disk ($R_c<5'$). The value of μ/σ_μ accordingly decreases and becomes less efficient in rejecting field stars, which makes their contamination a function of magnitude and distance to M81. The magnitude trend is visible in Table 9 as the fraction of stars retained to $(\mu/\sigma_\mu)_*$, $(1-f_*)$ increasing with magnitude at $R_c>15'$. However, the spatial variation occurs principally between objects inward and outward of $R_c=5'$; thus, the magnitude trend can be treated separately for the two regions at $R_c<5'$ and $R_c>5'$.

Away from the bright disk background ($R_c>5'$), the correct GCLF is the candidate luminosity function to which a control LF is subtracted. The control region is chosen to lie well away from M81, at $R_c>15'$. This operation removes the trend seen in Table 9 because both functions are identically affected, since they reside outward of 5′. However, this would not be the case at $R_c \leq 5'$, because at a given magnitude σ_μ is generally larger and μ/σ_μ lower than further out. Since the control LF was constructed at $R_c \gg 5'$, it does not reflect the inner variation of $(1-f_*)$ with V. More precisely, the value of $(\mu/\sigma_\mu)_*$ is less selective at $R_c<5'$ and is effectively raised to $(\mu/\sigma_\mu)_{*,\mathrm{Eff}}$. The effective limit is found, as a function of magnitude, by weighting $(\mu/\sigma_\mu)_*$ with the ratio of σ_μ(inner) to σ_μ(outer) at a given magnitude range. This procedure is summarized in Table 10, which gives the ratio of σ_μ between the inner and outer regions, the corresponding $(\mu/\sigma_\mu)_{*,\mathrm{Eff}}$, and the relative efficiency in excluding field objects. The *control* LF at $R_c \leq 5'$ is modified to account for this effect; the details of this procedure are outlined in the Appendix.

3.6.3 Supergiants

At $M_V \sim -8$, globular clusters and FGK type (yellow) supergiants have overlapping colors and magnitudes. Thus, supergiants in M81 could be included among the globular candidates, since they would also satisfy the low μ/σ_μ criteria. The relatively blue color of the progenitor to SN 1993J, $B-V \simeq 0.9$, first identified by Perelmuter (1993b), has demonstrated their presence. In this section, we assess their likely contamination of the list of candidates.

The number of yellow supergiants as a function of magnitude in M81 can be estimated from the ratio of FGK to OBA supergiants, r, in OB associations and the "blue plume" population (Sec. *3.3*) seen in M81. This ratio was observed by Meylan & Maeder (1983) in the Milky Way, and can be estimated using the spectral type–M_V diagram of the LMC provided by Humphreys & Davidson (1979; Fig. 2). We limited the analysis to $M_V \leq -7$, corresponding to the magnitude limit of the M81 sample, $V \leq 21$. The galactic and LMC associations give the same ratio of yellow to blue supergiants, $r \simeq 0.06$. The fainter objects in the CMD of the M81 field [Fig. 8(b)] have $V \leqslant 21$; if these objects were part of M81, they would have $M_V < -7$. At such magnitudes, only supergiants, compact OB associations, and globular clusters could be visible in M81. Therefore, the ratio of yellow to blue supergiants is an upper limit to the ratio of yellow supergiants to blue plume objects in M81.

In M81, the blue plume population to $V \leqslant 21$ is N(Plume) $=269$, which would imply ~ 16 FGK type supergiants. However, we limited to a handfull their contamination by excluding objects projected over the spiral arms, where supergiants are found [see Berkhuijsen & Humphreys (1989) on M31]. Using our 1983 CFHT plate (No. A3664, see Table 1) which suffers from 0.7″ seeing only, 24 candidates were rejected based on their location in or near "knots" in M81's spiral arms. Of those, nearly half were nonstellar and are probably OB associations dominated by a yellow supergiant. Therefore, the resulting candidate list has a negligible contamination from the supergiant population in M81.

4. THE SEARCH FOR GLOBULARS

4.1 Nonstellar Candidates

On deep exposures, bright M31 globulars ($d = 0.7$ Mpc) can be traced over diameters of 5–10 arcsec, which corresponds to 20–40 pc. Their aspect is typically diffuse and generally circular with a prominent central concentration. At M81 ($D_{M81} \simeq 3.2$ Mpc), such clusters would extend over diameters of $\sim 1''$ to $2''$ and could be distinguished from stars under excellent seeing conditions. Yet, from the spectra of 23 globular candidates selected on the basis of their visual appearance, Brodie & Huchra (1991) found 15 to be distant galaxies or H II regions. A large fraction of these extraneous objects can be excluded on the basis of accurate BVR colors alone (van den Bergh 1985; Reed *et al.* 1992), now available for the M81 field. A CFHT plate (No. 3664, Kodak IIIaF emulsion+Schott GG495 filter, $\lambda_{\rm eff} = 610$ nm, 60 min exposure, $55' \times 55'$ FOV) taken on 1983 December 31 in 0.7″ FWHM seeing (Puche 1986) was searched for objects that appeared "globular-like," i.e., slightly diffuse, circular, with central concentration. We identified a total of 171 such objects. All have $V < 21.2$, well above the plate limit at $V = 23.5$ (Puche 1986), which suggests our visual ability to detect globular-like images is limited to $V \simeq 21$ mag on this plate.

A similar problem of globular appearance and detectability occurred in the case of NGC 5128 (Centaurus A) because it is located at a similar distance from the Milky Way as M81, D(NGC 5128)~ 3 Mpc (Hesser *et al.* 1984, hereafter referred to as HHVH). A good review of the saga surrounding the detection in NGC 5128 of the first to ≈ 600 globular clusters is given by HHVH. Three points should be noted regarding the confirmed globulars in NGC 5128 that were selected on the basis of image structure and $(B-V)$. Firstly, their magnitudes are consistent with bright Milky Way globulars, $M_V \sim -9$. Thus, our magnitude selection [Eq. (8)] is justified here too. Secondly, their high success rate, although in part fortuitous, supports the use of $(B-V)$ as an efficient way to minimize contamination from background galaxies. Thirdly, the angular size of the clusters appears to increase with galactocentric distance to NGC 5128. Therefore, and as noted by HHVH, samples selected on visual appearance are vulnerable to magnitude and dynamical bias. For example, clusters with orbits that do not result in tidal stripping by the disk may be favored in the selection process.

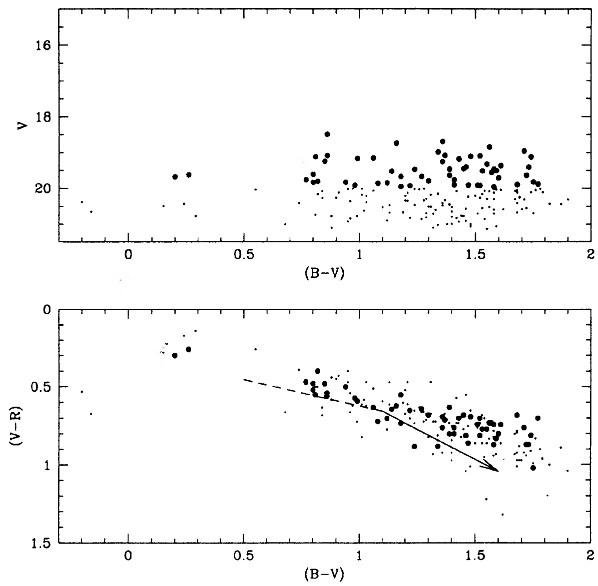

FIG. 9. The color–color and color–magnitude diagrams for globular-like images. Filled circles have $V<20$ and dots have $V \geqslant 20$. In the color–color plot, the locus of galactic globulars [reddened by $E(B-V)=0.1$] is shown as a dashed line, and a reddening vector is represented by an arrow.

The color–magnitude and color–color diagrams for the globular-like objects in M81 are shown in Figs. 9(a) and 9(b), where filled circles have $V \leqslant 20$ and dots have $V > 20$ mag. Also shown is the locus of galactic globulars to which is applied the foreground reddening towards M81 (heavy dash line), and a reddening vector (solid arrow). The sample is largely dominated by red objects ($B-V > 1.0$), most of which are probably background galaxies. We also note the presence of seven diffuse objects with $(B-V) < 0.50$. All of the latter are situated within $10'$ of the center of M81 and the two bluest in $(B-V)$ exhibit a $(V-R)$ excess which suggests they may be core clusters in H II regions, (the IIIaF sensitivity includes Hα).

The radial distribution of the globular-like images is shown in Fig. 10 for a sequence of BVR selections. The sample in Fig. 10(a) spans the color range expected for M81 globulars as given in Eqs. (14)–(16). In Fig. 10(b), we applied BVR criteria for disk reddened candidates given in Eqs. (17)–(19); all other objects are shown in Fig. 10(c). Both foreground reddened and disk reddened samples [Figs. 10(a) and 10(b)] exhibit a marginally significant excess at $R_c < 10'$ of N(excess)$=11 \pm 4$ and 8 ± 3, respectively. The surface density of sample (c) exhibits an insignificant excess, as expected in the case of background galaxies.

In summary, we have determined that the sample of globular-like objects is largely dominated by background galaxies at $(B-V) > 1.1$. There are 19 ± 7 globulars with

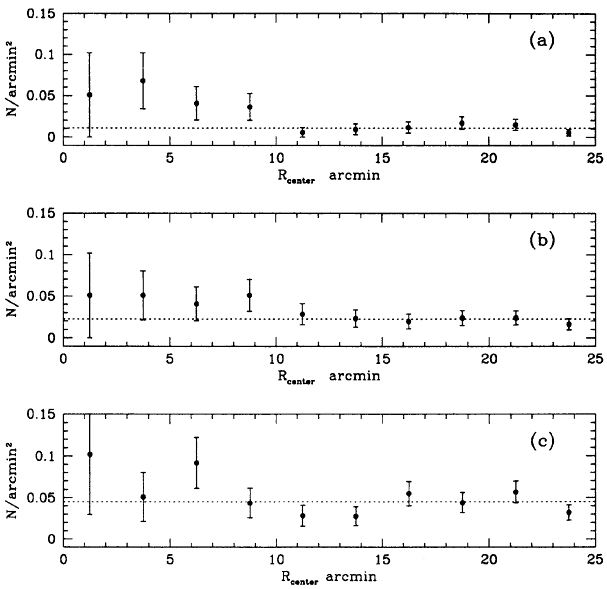

FIG. 10. The surface density vs distance from M81 diagram for a sequence of color–magnitude selections: (a) galactic-like: $V \geq 18$, $B-V=0.5-1.1$, $V-R=0.3-0.7$; (b) disk reddened: $V \geq 19.6$, $B-V=0.9-1.5$, $V-R=0.6-1.0$; (c) all others.

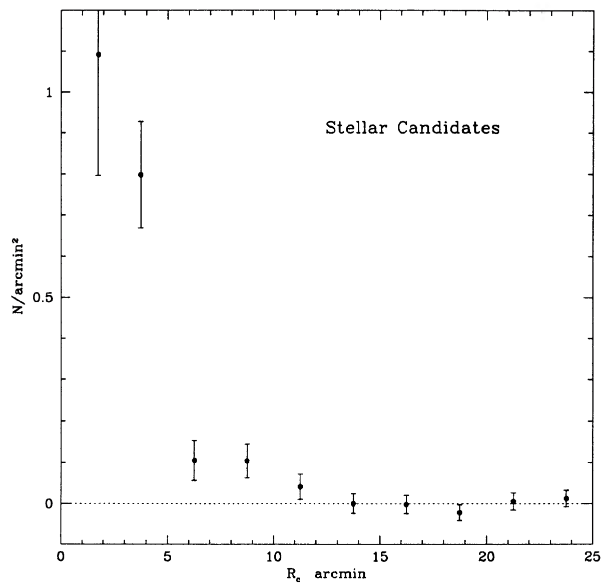

FIG. 11. The surface density as a function of radius for star-like globular cluster candidates. A clear excess is detected at $R_c < 12.5' \simeq 11$ kpc.

galactic-like BVR features and appearance at $R_c < 10'$. Given the size of the galactic and M31 GCS's, $N_T = 200-300$, the majority of M81 globulars must therefore appear stellar in this survey.

4.2 *Candidates with a Stellar Profile and the M81 Globulars*

4.2.1 Spatial distribution and total population

The radial distribution of candidates that have a star-like point spread function, and with $V \geq 18$, $0.5 \leq (B-V) \leq 1.1$, and $0.3 \leq (V-R) \leq 0.7$, is shown in Fig. 11, constructed according to the precepts of Sec. *2.4* and developed in the Appendix. A strong excess can be seen rising towards the center of M81. In the region $2' \leq R_c \leq 12.5'$, the excess is 74 ± 11 objects out of 116 candidates, implying a 63% mean success rate; at $R_c \leq 10'$ it increases to 72%.

The radial profile combining both *star-like* and *nonstellar* candidates is shown in Fig. 12; the least squares fit,

$$\log(N/\text{sq arcmin}) = -2.07 \log_{10}(R_c') + 0.82 \pm 0.05, \tag{15}$$

is plotted as a solid line. Since the scaling factor in this $\sim R^{-2}$ relation is distance invariant, we can derive the relative populations in M81 and the galaxy by comparing their respective scaling factors. This scaling does not require interpolating towards the center of M81 and the Milky Way. After correcting for incompleteness in magnitude (17%) and for the μ/σ_μ tail distribution (10%), we find a total population of $N_T = 210 \pm 30$ globular clusters in M81. Since $N_T \simeq 150$ in the galaxy, $N_T(\text{M81})/N_T(\text{galaxy}) = 1.4 \pm 0.2$. For comparison, the ratio of the squares of the rotation curve amplitudes (i.e., mass) in M81 (Rots 1975) and in the Milky Way (Schmidt 1985) is: $\mathcal{M}_{\text{M81}}/\mathcal{M}_{\text{MW}} \propto (250 \text{ km s}^{-1}/220 \text{ km s}^{-1})^2 = 1.3$. The similar ratios suggest a similar fractional mass in the form of globular clusters in M81 and the Milky Way, and thus M31 (Racine 1991).

4.2.2 The M81 GCLF

The M81 GCLF was constructed, following the precepts of Sec. *2.4* and developed in the Appendix, for the "*excess*"

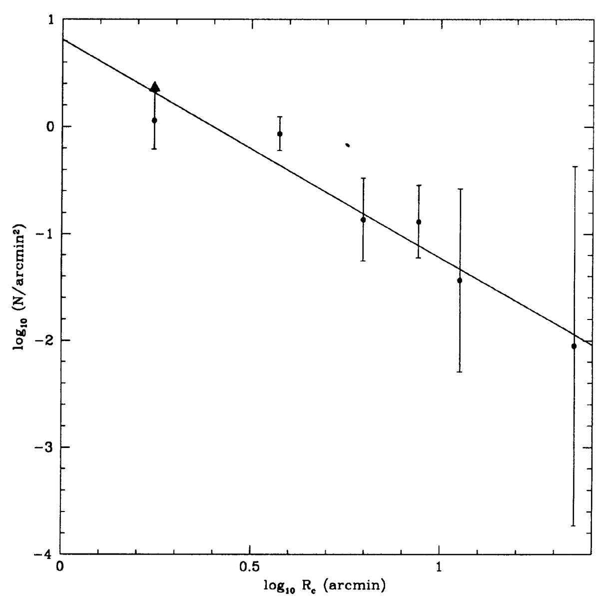

FIG. 12. The log–log plot of Fig. 11 used to estimate the total population. The filled triangle is the inner surface density corrected for the estimated number of globulars located behind the disk of which only 13 ± 5 are visible (cf. Sec. *4.2.3*).

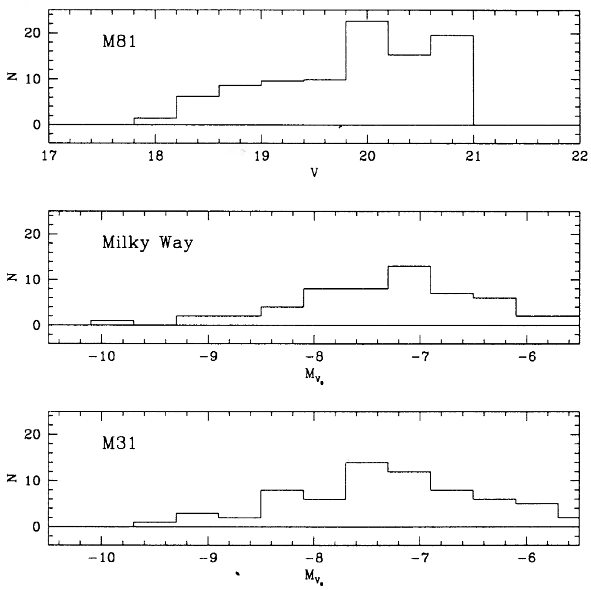

FIG. 13. The luminosity function of the M81 globular candidates with $18 \leqslant V \leqslant 21$ (top), corrected according to the procedure set out in the Appendix. The Milky Way and M31 halo GCLF are also shown (middle and bottom, respectively). The horizontal scales are aligned for $(m-M)_0^{\rm M81}=27.5$.

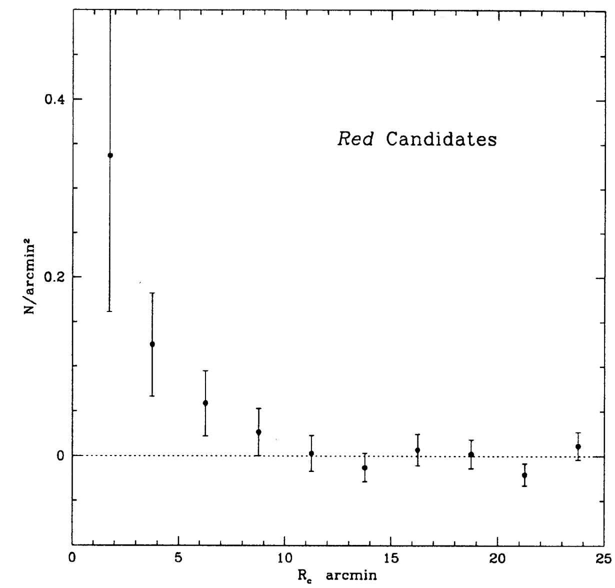

FIG. 14. The surface density as a function of radius of objects with disk-reddened-like color and magnitude. A net excess is apparent at $R_c < 10'$.

region $2' \leqslant R_c \leqslant 12.5'$ (see Fig. 11); the control area is located at $15' \leqslant R_c \leqslant 25'$. In Fig. 13 we show the M81 GCLF to the Milky Way and M31 halo GCLFs. We utilize the halo samples, albeit their small size, because they are >90% complete and to minimize errors due to uncertain A_V estimates in the galactic plane (the M31 disk sample, for example, is limited to $V \lesssim 17$ which corresponds to $M_V \lesssim -7.5$). Different bin sizes and shifts in the binning sequence showed that the maximum of the M81 GCLF is located at $20.0 \leqslant V^* \leqslant 20.6$ mag, or $V^* = 20.3 \pm 0.3$. Assuming $(m-M)_0 = 27.5 \pm 0.3$ and A_V(foreground)$=0.3 \pm 0.1$, the peak of the M81 GCLF occurs at $M_V^*(\text{M81}) = -7.5 \pm 0.4$, the same location as that of the Milky Way and M31 systems. In effect, Fig. 13 shows a striking resemblance between the M81, Milky Way, and M31 GCLFs.

4.2.3 *The effect of the disk*

The radial distribution of *star-like* objects, with the colors and magnitudes expected of globulars seen through the disk, is shown in Fig. 14. There is an excess of 13 ± 5 objects at $2' \leqslant R_c \leqslant 7.5'$; this range coincides with the size of the M81 disk. If these are globulars seen through the M81 disk, then correcting for incompleteness in V and μ/σ_μ, there should be 76 ± 29 globulars behind the M81 disk at $2' \leqslant R_c \leqslant 7.5'$. In the same annulus, the excess of galactic-like candidates (e.g., foreground reddened only) is 92 ± 14 objects, consistent with a symmetric distribution of globulars.

4.2.4 *Color and metallicity distributions*

We plot in Figs. 15(a)–15(c) the $(B-V)_0$ and $(V-R)_0$ control-subtracted distributions for candidates at $2' \leqslant R_c \leqslant 12.5'$; a foreground reddening of $E_{(B-V)} = 0.1$ was applied to the color bins. Although the color indices have been restricted to specific ranges [cf. Eq. (14)–(16)] the brackets are 6σ wide. This enables a fair description of the distribution functions. The MW, M31, and M81 color distributions have a similar morphology and scatter about the same mean indices (cf. Table 7 and Fig. 2 of Racine 1991), which suggests similar metallicity distributions. Using the relation of Reed *et al.* (1994) between [Fe/H] and $(B-R)_0$ for galactic globular clusters,

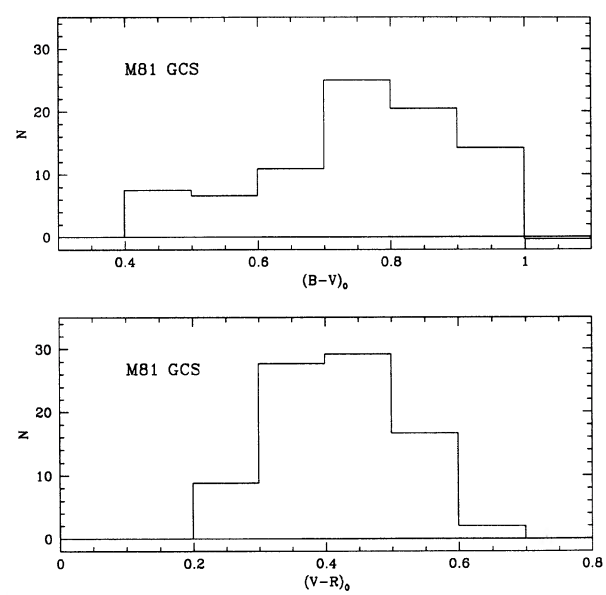

FIG. 15. Color distribution for M81 candidates. The $(B-V)_0$ index is highly correlated to metallicity and shows a larger spread than $(V-R)_0$, which is not as good a metallicity indicator (Reed *et al.* 1994).

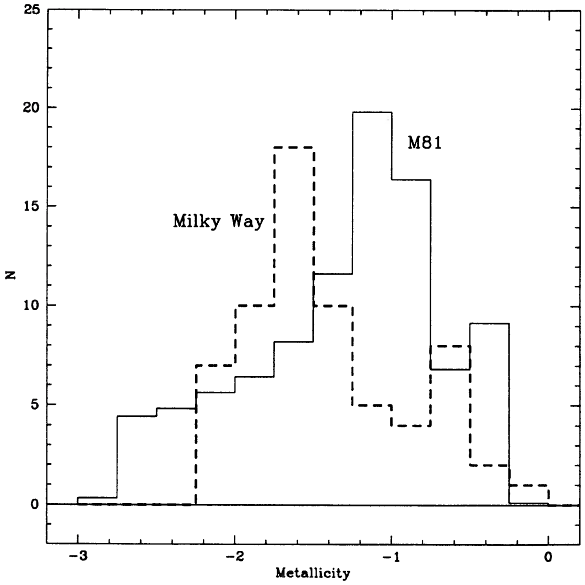

FIG. 16. The metallicity histogram for the M81 GCS, where $[Fe/H]=f(B-R)_0$ (solid line), is compared to that of Milky Way clusters in the range 2 to 11 kpc (dashed line).

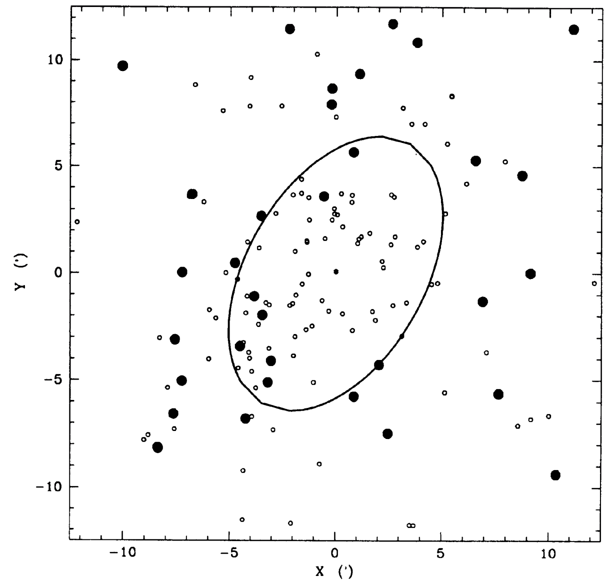

FIG. 17. The projection of globular cluster candidates onto the sky. Symbols are: $*$=center of M81, filled circles=candidates with $[Fe/H]<-2$, open circles=$[Fe/H]>-2$.

$$[Fe/H]=3.11(B-R)_0-4.97, \qquad (16)$$

we derive a (control-subtracted) photometric metallicity distribution which we show in Fig. 16; the bin size of 0.25 dex corresponds to the uncertainties in the metallicity estimates. For comparison, we also show the metallicity distribution of Milky Way globulars projected in the same galactocentric range. For the M81 system, a sharp mode occurs at $[Fe/H]_{B-R}\simeq-1.0$ above a rather uniform distribution for $-2.7<[Fe/H]_{B-R}<-0.3$. The disk–halo dichotomy is not visible there, but can be seen in the Milky Way sample. However, uncertainties in the mapping of $(B-R)_0$ to $[Fe/H]_{B-R}$ could be responsible for a smoothing of the M81 metallicities. In effect, the peak of the M81 distribution coincides with the mean abundance between the metal-rich and metal-poor Milky Way globulars, in the 2 to 11 kpc range. There are 15 candidates with $[Fe/H]<-2$; such objects in the galaxy are located away from the disk, and few have been detected in M31. The projection in the sky of *all* candidates is shown in Fig. 17, where filled circles have $[Fe/H]<-2$ and open circles have $[Fe/H]>-2$. Candidates were limited to $R_c\leq 12.5'$, where an excess is visible, and thus, globulars should dominate the population. Most metal-poor candidates lie outside of the M81 disk, whereas their richer counterpart fill the entire area. A weak correlation is found between the mean (control-subtracted) metallicity and distance to M81, as shown in Fig. 18; the weighted least squares fit gives

$$[Fe/H]=-0.05(\pm0.04)R_c(\mathrm{kpc})-1.00(\pm0.01) \qquad (17)$$

plotted as a solid line. If this were due to reddening by the disk, Fig. 18 would imply an excess $E(B-V)\simeq0.2$ at $R_c<3$ kpc. This value compares well with the mean reddening over the M81 disk estimated in Sec. *3.3*. Assuming half the population at $R_c<3$ kpc were located behind the disk, then the overall average magnitude in V should be dimmed by $A_V\simeq0.6$ mag there. However, Fig. 19 shows the corrected average luminosity of candidates brightens at inner radii, contrary to the expected behavior of disk reddened objects. Therefore, the inner sample must be dominated by intrinsi-

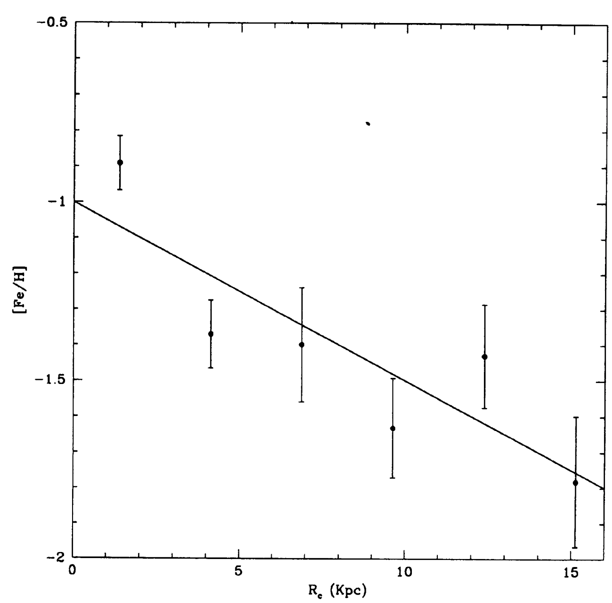

FIG. 18. Metallicity vs distance from M81. The least square fit is shown as a solid line; a slight trend is visible.

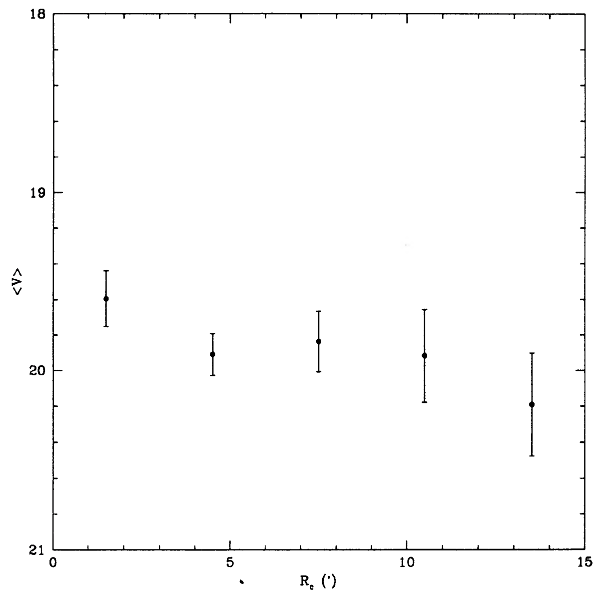

FIG. 19. The corrected average luminosity vs distance to M81. For each annulus, a corrected star-like plus nonstellar candidates luminosity function was constructed, from which an average was derived.

cally red objects, possibly more metal rich as well. Such a trend is also observed in the galaxy out to 100 kpc and in M31 to 20 kpc (Harris & Racine 1979; Huchra *et al.* 1991; Reed *et al.* 1994).

4.3 Conclusion

We have employed an extensive photometric and astrometric database to extract statistical information on the M81 GCS. The system is observed as an excess of objects satisfying our globular cluster selection criterion over the background density to $R_c = 12.5'$ or 11 kpc, (the disk extends to 7 kpc). The M81 GCS appears much similar to its Milky Way and M31 counterpart in its population, spatial extent, and BVR parameters. The total population is estimated at $N_T = 210 \pm 30$. The GCLF reaches its maximum at $V^* = 20.3 \pm 0.3$ mag, which is marginally brighter than expected for $M_V^* = -7.5$ and the Cepheids distance of Madore *et al.* (1993) and Freedman *et al.* (1994). However, we also showed that small but significant trends are present in their photometry, and we suggest a revision of the distance modulus to $(m-M)_0^{\rm M81} = 27.5 \pm 0.3$. Assuming this corrected distance modulus, the M81, M31, and Milky Way GCLFs reach their peak at the same location, $M_V^* = -7.5$. Finally, the $(B-V)_0$ and $(V-R)_0$ distributions are remarkably similar to those in the MW and M31 and indicate similar ranges in metallicity.

The metallicity index $[\mathrm{Fe/H}] = f(B-R_0)$ exhibits a strong peak at $[\mathrm{Fe/H}] = -1.0$ with a tail of metal poor objects. A weak correlation is observed between [Fe/H] and galactocentric radius, R_c; most objects with $[\mathrm{Fe/H}] < -2$ are projected outside the disk. If the metallicity index traces the enrichment history of the protogalactic gas, then the outer subsystem was formed prior to the metal enrichment of the disk system, which continuously collapsed inward. That evidences for this scenario also appear in the Milky Way and in M31 suggests it may be typical to the formation process of early type spirals.

The authors wish to thank the referee, G. L. H. Harris, for a particularly enlightening review of this paper. J.-M.P. is grateful to the Université de Montréal for providing travel expenses and ample computer support, and to ARTIFEX-Belgique for a generous grant. This research was supported in part through grants from the Natural Sciences and Engineering Research Council, Canada and from Fonds FCAR, Québec.

APPENDIX: REMOVING THE BIAS

We now lay the mechanics enabling the construction of luminosity and radial distributions. It consists in a direct application of the concept outlined in Sec. *3.6.2*, namely removing the magnitude trend at $R_c > 5'$ using Table 9 and at $R_c \leq 5'$ using Table 10. Mathematically, this is possible by organizing object counts into entries in a magnitude–radial distance matrix. Each entry, corresponding to a particular magnitude bin and radial distance range, may be scaled utilizing the appropriate table (8 or 9). To directly remove any trend with magnitude, a control matrix is constructed based on the same selection, but limited to a distance range safely away from M81. The corrected matrix is the subtraction of the control matrix from the candidate matrix. It is further scaled to account for incompleteness.

Consider the following matrix where each entry is the number of candidates in a specific magnitude–distance range,

$$N(V,R_c) = \left(\begin{array}{ccccc} V & & R_c \text{ arcmin}\rightarrow & & \\ \downarrow & 0-2.5 & 2.5-5.0 & \ldots & 22.5-25.0 \\ V=17.6\pm0.2 & n_{1,1} & n_{2,1} & \ldots & n_{10,1} \\ V=18.0\pm0.2 & n_{1,2} & n_{2,2} & \ldots & n_{10,2} \\ \vdots & \vdots & \vdots & \ddots & \vdots \\ V=20.8\pm0.2 & n_{1,9} & n_{2,9} & \ldots & n_{10,9} \end{array} \right). \tag{A1}$$

The candidate matrix, $N_{\rm can}(V,R_c)$, has the form of Eq. (A1) but the last column extends to $R_c \leqslant R_{\rm lim}$, instead of $R_c \leqslant 25$ arcmin, to account for the spatial range of candidates away from M81. Conversely, the control matrix, $N_{\rm ctrl}(V,R_c)$, is limited to a distance range safely beyond that of globulars. This matrix will be subtracted from the candidate matrix after scaling. This is an important step because it addresses the biases noted in the Sec. *3.6.2*, namely that the efficiency of the μ survey is lower for fainter objects and for those within 5 arcmin of the center of M81. The subtraction of the control matrix removes the magnitude bias at $R_c > 5$ arcmin because both matrices are similarly affected there. But at closer distances of M81, the lower efficiency of rejection is present only in the candidate matrix so that the raw control matrix underestimates the number of objects to subtract (at $V > 18.75$). At a given magnitude V, this is accounted for by scaling (up) the control function with the fractional inclusion of field objects at $R_c \leqslant 5'$ compared to that at $R_c > 5'$, $(1-f_*)_{{\rm Eff},V}/(1-f_*)_V$:

$$\Delta N(V,R_c) = N_{\rm can}(V,R_c) - \begin{pmatrix} \sum_{R_c=20'}^{25'} N_{\rm ctrl}(V=17.6\pm0.2,R_c) \\ \vdots \\ \sum_{R_c=20'}^{25'} N_{\rm ctrl}(V=20.8\pm0.2,R_c) \end{pmatrix}$$

$$\cdot \begin{pmatrix} & R_c=0'\text{–}2.5' & 2.5'\text{–}5.0' & 5.0'\text{–}7.5' & \dots \\ V=17.6\pm0.2 & \frac{(1-f_*)_{{\rm eff},V}}{(1-f_*)_V} & \frac{(1-f_*)_{{\rm eff},V}}{(1-f_*)_V} & 1.0 & \dots \\ \dots & \dots & \dots & \dots & \dots \\ V=20.8\pm0.2 & \frac{(1-f_*)_{{\rm eff},V}}{(1-f_*)_V} & \frac{(1-f_*)_{{\rm eff},V}}{(1-f_*)_V} & 1.0 & \dots \end{pmatrix} \frac{A_{\rm can}}{A_{\rm ctrl}}, \qquad \text{(A2)}$$

where $A_{\rm can/ctrl}$ are the areas covered by the respective sampling regions. Summing the columns of the *control* matrix (placed on the left) collapses it into a 1D vector, while the matrix scaling this *control* vector (on its right) is of the same rank as $N_{\rm can}(V,R_c)$; the product in Eq. (2) should be understood as a dot product resulting in a matrix of identical rank as the candidate matrix.

The difference of the candidate and the scaled *control* matrices is furthermore corrected for the fraction of objects with $n_{\rm plates}$ at V and it is rescaled to account for globulars that have $\mu/\sigma_\mu \geqslant 2.75$. This gives an equation of the form,

$$N_{\rm gc}(V,R_c) = \Delta N(V,R_c) \cdot \begin{pmatrix} f(n_{\rm plates}, V=17.6\pm0.2 \\ \vdots \\ f(n_{\rm plates}, V=20.8\pm0.2) \end{pmatrix}$$

$$\times C_{\mu/\sigma_\mu \geqslant 2.75} C_{B-V} C_{V-R}, \qquad \text{(A3)}$$

where $f(n_{\rm plates},V)$ is the inverse of the fraction of objects found on at least $n_{\rm plates}$ at magnitude V, cf. Table 5. Here also the multiplicative operation of the difference matrix with the scaling matrix is a dot product. No variation of $f(n_{\rm plates},V)$ with distance was observed, which makes it a 1D vector as opposed to a matrix.

Adding the columns of Eq. (3) collapses the matrix one-dimensionally to the luminosity function and adding up the rows gives the number of objects as a function of distance from M81. These results are applied in Sec. *4.2*.

REFERENCES

Armandroff, T. E. 1989, AJ, 97, 375

Ashman, K. M., & Zepf, S. E. 1992, ApJ, 384, 50

Battistini, P., Bonoli, F., Braccesi, A., Federici, L., Fusi Pecci, F., Marano, B., & Borngen, F. 1987, A&AS, 67, 447

Belov, V. N. 1993, in The Globular Cluster–Galaxy Connection, edited by G. Smith and J. Brodie (ASP, San Francisco), PASP Conf. Ser. Vol. 48, p. 800

Berkhuijsen, E. M., & Humphreys, R. M. 1989, A&A, 214, 68

Bohlin, R. C., Savage, B. D., & Drake, J. F. 1978, ApJ, 224, 132.

Brodie, J., & Huchra, J. 1991, ApJ, 379, 157

Brodie, J. 1993, in The Globular Cluster–Galaxy Connection, edited by G. Smith and J. Brodie (ASP, San Francisco), ASP Conf. Ser. Vol. 48, p. 483

Brown, J. H., Burkert, A., & Truran, J. W. 1991, ApJ, 376, 115

Bruzual, G. A., Peimbert, M., & Torres-Peimbert, S. 1982, ApJ, 260, 495

Burstein, D., & Heiles, C. H. 1984, ApJS, 54, 33

Eggen, O. J., Lynden-Bell, D., & Sandage, A. R. 1962, ApJ, 136, 748

Djorgovski, S., & Santiago, B. X. 1992, ApJ, 391, L5

Fisher, P., Hesser, J. E., Harris, H. C., & Bothun, G. D. 1990, PASP, 102, 5

Flower, P. J. 1977, A&A, 54, 31
Freedman, W. L., & Madore, B. F. 1988, ApJ, 332, L63
Freedman, W. L., *et al.* 1994, ApJ, 427, 628
Hanson, R. B. 1987, AJ, 94, 409
Harris, W. E. H., & Racine, R. 1979, ARA&A, 17, 241
Hesser, J. E., Harris, H. C., van den Bergh, S., & Harris, G. L. H. 1984, ApJ, 276, 491
Huchra, J. 1993, in The Globular Cluster–Galaxy Connection, edited by G. Smith and J. Brodie, (ASP, San Francisco) ASP Conf. Ser. Vol. 48, p. 483
Huchra, J., Brodie, J., & Kent, S. 1991, ApJ, 370, 495
Humphreys, R. M., & Davidson, K. 1979, ApJ, 232, 409
Humphreys, R. M., Aaronson, M., Lebofsky, M., McAlary, C. W., Strom, S. E., & Capps, R. W. 1986, AJ, 91, 808
Humphreys, R. M., & Aaronson, M. 1987, AJ, 94, 1156
Jacoby, G. H., Ciardullo, R., Ford, H. C., & Booth, J. 1989, ApJ, 344, 704
Kaufman, M., Bash, F. N., Kennicutt Jr., R. C., & Hodge, P. W. 1987, ApJ, 319, 61
Klemola, A. R., Jones, B. F., & Hanson, R. B. 1987, AJ, 94, 501
Madore, B. F., Freedman, W. L., & Lee, M. G. 1993, AJ, 106, 2243
Massey, P., Garmany, C. D., Silkey, M., & Degioia-Eastwood, K. 1989a, AJ, 97, 107
Massey, P., Parker, J. W., & Garmany, C. D. 1989b, AJ, 98, 1305
Mathis, J. S. 1990, ARA&A, 28, 37
McLaughlin, D. E., Harris, W. E., & Hanes, D. A. 1994, ApJ, 422, 486
Mendez, R. 1994, private communication
Metcalfe, N., & Shanks, T. 1991, MNRAS, 250, 438
Meylan, G., & Maeder, A. 1983, A&A, 124, 84
Moffat, A. F. J. 1969, A&A, 3, 455
NOAO Newsletter, March 1990
Perelmuter, J.-M. 1993a, in The Globular Cluster-Galaxy Connection, edited by G. Smith and J. Brodie (ASP, San Francisco), ASP Conf. Ser. Vol. 48, p. 580
Perelmuter, J.-M. 1993b, IAUC 5736
Perelmuter, J.-M., Brodie, J., & Huchra, J. 1995, in preparation
Puche, D. 1986, Masters thesis, Université de Montréal
Racine, R. 1991, AJ, 101, 865
Racine, R., & Harris, W. E. 1989, AJ, 98, 1609
Racine, R., & Harris, W. E. 1992, AJ, 104, 1068
Racine, R., & Perelmuter, J.-M. 1995, in preparation (Paper II)
Reed, B. C., Hesser, J. E., & Shawl, S. J. 1988, PASP, 100, 545
Reed, L. G., Harris, G. L. H., & Harris, W. E. 1994, AJ, 104, 555
Reed, L. G., Harris, G. L. H., & Harris, W. E. 1992, AJ, 103, 824
Rots, A. H. 1975, A&A, 45, 43
Sandage, A. 1990, JRASC, 84, 70
Sandage, A. 1984, AJ, 89, 621
Searle, L., & Zinn, R. 1978, ApJ, 225, 357
Schild, R., & Oke, J. B. 1971, ApJ, 169, 215
Schmidt, M. 1985, in The Milky Way, IAU Symposium No. 106, edited by H. van Woerden, R. J. Allen, and W. B. Burke P. Hut (Reidel, Dordrecht), p. 75
Secker, J. 1992, AJ, 104, 1472
Stetson, P. B. 1987, PASP, 99, 191
van den Bergh, S. 1985, ApJ, 297, 361
van den Bergh, S. 1991, PASP, 103, 1053
Wyse, R. 1992, private communication
Zickgraf, F., & Humphreys, R. M. 1991, AJ, 102, 113
Zinn, R. 1990, JRASC, 84, 89